

AperTO - Archivio Istituzionale Open Access dell'Università di Torino

**NiO/ZrO<sub>2</sub> nanocomposites as photocathodes of tandem DSCs with higher photoconversion efficiency with respect to parent single-photoelectrode p-DSCs**

**This is the author's manuscript**

*Original Citation:*

*Availability:*

This version is available <http://hdl.handle.net/2318/1803915> since 2021-09-22T13:36:15Z

*Published version:*

DOI:10.1039/d1se00566a

*Terms of use:*

Open Access

Anyone can freely access the full text of works made available as "Open Access". Works made available under a Creative Commons license can be used according to the terms and conditions of said license. Use of all other works requires consent of the right holder (author or publisher) if not exempted from copyright protection by the applicable law.

(Article begins on next page)

# NiO/ZrO<sub>2</sub> nanocomposites as photocathodes of tandem DSCs with higher photoconversion efficiency with respect to parent single-photoelectrode p-DSCs

Matteo Bonomo,<sup>\*a,b</sup> Emmanuel J. Ekoj,<sup>c</sup> Andrea G. Marrani,<sup>a</sup> Ana Y. Segura Zarate,<sup>b</sup> Denis P. Dowling,<sup>c</sup> Claudia Barolo,<sup>b,d</sup> and Danilo Dini <sup>\*a</sup>

## DISCLAIMER

**THIS DOCUMENT IS THE NOT PAGINATED VERSION OF THE ARTICLE: “NiO/ZrO<sub>2</sub> nanocomposites as photocathodes of tandem DSCs with higher photoconversion efficiency with respect to parent single-photoelectrode p-DSCs”. PLEASE DOWNLOAD THE FINAL PAGINATED VERSION AT <https://pubs.rsc.org/en/content/articlelanding/2021/SE/D1SE00566A>**

The nanocomposites of nickel oxide (NiO) and zirconia (ZrO<sub>2</sub>) (NZNCs) are particularly effective photocathodic materials in p-type dye-sensitized solar cells (p-DSCs) and tandem DSCs (t-DSCs). The t-DSCs obtained from P1-sensitized NZNC as photocathode and nanostructured titania (TiO<sub>2</sub>) sensitized with squaraine VG10-C8 as photoanode display overall efficiencies of ca. 2 % at their best and, more importantly, produced photocurrents that surpassed systematically the values obtained from the parent devices having one photoelectrochemical interface. Such a finding is a consequence of the diminished resistance of the electrolyte the thickness of which is systematically smaller in t-DSCs with respect to parent DSCs with a single photoelectrochemical junction and same interelectrode separation. The results here reported demonstrate that a careful combination of photoelectroactive electrodes can lead to an increase in current density of more than 15% in the t-DSC with respect to single-junction DSCs employing the same photoelectrodes provided that the whole thickness of the t-DSC is the same as in the single photoelectrode DSC and the photoelectrodes in the t-DSC do not incur in short-circuit phenomena through the electrolyte. For the successful realization of t-DSCs another important aspect is the complementarity of the absorption properties of the chosen colorants with the sensitized electrodes having similar absorbance in their respective ranges of optical absorption. The latter condition in t-DSCs makes possible the achievement of photoactivity spectra with a uniform efficiency of conversion in the whole visible range. For the attainment of efficient t-DSCs the two different photoelectrodes from parent DSCs (i.e. the devices at a single photoelectrochemical interface), should generate anodic and cathodic photocurrent densities with very similar values. Such a matching of photocurrents requires a careful selection of the thickness values for the photoelectrodes especially in case of materials with considerably different characteristics of charge injection. The approach here considered is a promising one for the assembly of quasi-transparent photoelectrochemical tandem devices operating as smart windows that convert light into electrical

power.

## Introduction

At the basis of the research on dye-sensitized solar cells (DSCs)<sup>1-5</sup> there is the main motivation of realizing a photovoltaic device with (partial) optical transparency.<sup>6,7</sup> Such a type of photoconversion system is particularly attractive for the smart fenestration of buildings,<sup>8-10</sup> as well as for the development of indoor light-activated powering devices that require low levels of luminous input.<sup>11</sup> In the same device the realization of the dual function of (i) transmitting the visible portion of the incident

light, and (ii) converting efficiently the NIR remainder of the incident light into electricity constitutes certainly a truly important technological achievement with strong impact on the capability of satisfying the growing demand of energy in a sustainable way.<sup>12</sup>

DSCs present three different configurations: *n*-type,<sup>13,14</sup> *p*-type<sup>15</sup> and tandem (*t*-).<sup>16–19</sup> In the first two types of photoelectrochemical cells the classification is based on the nature of the semiconducting electrodes with nanostructured features whilst in the third case of *t*-DSC both mesoporous electrodes are photoelectrochemically active.<sup>17</sup> In *n(p)*-DSCs the photoelectrochemically active electrode is a sensitized anode(cathode) at which the photoactivated process of oxidation(reduction) occurs.<sup>2</sup> A *t*-DSC can be straightforwardly assembled by coupling a photoanode of sensitized TiO<sub>2</sub> with a photocathode of sensitized NiO.<sup>15,20</sup> Therefore, in *t*-DSCs both components of the redox couple are involved in the photoactivated processes of electron transfer in which the sensitizers act as mediators. A consequence of the use of *t*-DSCs with one redox couple is the lack of dependence of the open circuit photovoltage (OCV,  $V_{oc}$ ) on the Nernst level of the redox couple. In fact, the value of  $V_{oc}$  in *t*-DSCs depends exclusively on the relative positions of the band edges of the two different semiconducting electrodes.<sup>17</sup> Theoretically, *t*-DSCs can achieve higher photoconversion efficiencies<sup>21,22</sup> and larger values of  $V_{oc}$  with respect to the parent DSCs with a single-photoelectrode. Combining two sensitized photoelectrodes in the same cell represents a meaningful approach at the condition that the two sensitizers possess complementary absorption features and similar dynamics of excitation.<sup>23–27</sup> The *t*-DSCs display always an increase of  $V_{oc}$ , as predicted, but this is generally accompanied by a decrement of the current density with the final result of lowering the overall efficiency in comparison to the corresponding parent *p*- and *n*-DSCs.

Indeed, the photoconversion performance of a tandem device is limited by the less performing photoelectrode of a DSC (typically the mesoporous photocathode). From one hand, mesoporous TiO<sub>2</sub>-based *n*-DSCs, i.e. the most efficient devices with single photoelectrode,<sup>28</sup> produce short circuit photocurrent density ( $J_{sc}$ ) approaching 20 mA cm<sup>-2</sup>,<sup>29</sup> while the record value of  $J_{sc}$  in a NiO-based *p*-DSC does not overcome 10 mA cm<sup>-2</sup> (this is achieved when the couple [Fe(acac)<sub>3</sub>]<sup>0/1-</sup> and PMI-6T-TPA are employed as redox shuttle and sensitizer, respectively).<sup>30</sup> The improvement of the overall photoelectrochemical performance in passing from the *t*-DSC to its parents *n*-DSC/*p*-DSC takes place if the single electrode devices produce similar photocurrents thus fulfilling the requirement of current density matching. The generally poorer performance of the photocathode in a *t*-DSC constitutes the main problem. Some authors have tackled that by defining more efficacious dye-sensitizers.<sup>26,31–36</sup> Particularly promising results have been obtained by Odobel and co-workers when blue thienyl-substituted diketopyrrolopyrrole dyes were used as sensitizers of *p*- and *t*-DSCs.<sup>34</sup>

Very high overall efficiencies ( $\eta$ ) of 0.35% and 4.10% were recorded for *p*- and *t*-DSC, respectively. In correspondence of these efficiencies the *p*- and *t*-DSC produced respectively 150 and 910 mV as values of  $V_{oc}$ , and 7.8 and 6.4 mA cm<sup>-2</sup> as values of  $J_{sc}$ . In the ambit of *p*-DSCs, the real state of art is represented by the photoelectrochemical cell with NiO deposited via screen-printing ( $l = 4.2 \mu\text{m}$ ) as mesoporous cathode and perylene–thiophene–triphenylamine (PMI–6T–TPA) as dye-sensitizer with the attainment of an unsurpassed maximum of efficiency equal to 2.51 %.<sup>30</sup> The record *p*-DSC developed by Spiccia *et al.*<sup>30</sup> employed the redox couple [Fe(acac)<sub>3</sub>]<sup>0/1-</sup> in acetonitrile being the anti-aggregating agent chenodeoxycholic acid (CDCA) present in the electrolyte. They also reported a remarkably high FF (0.60 and 0.51 under 0.1 Sun and 1 Sun respectively) when the iron-based electrolyte is employed; unfortunately, due to its high redox potential (0.4 V vs NHE) too close to the TiO<sub>2</sub> VB, it could not be implemented in tandem device when high efficient photoanode side is required. Other redox couples (i.e.

conventional I-based and Co-based electrolytes) lead to much lower FF ( $< 0.50$ ). Indeed, the limits of *p*-DSCs are evidenced through the recognition that *p*-DSCs generally display lower values of fill factor (FF)<sup>37–39</sup> in comparison to *n*-DSCs<sup>40,41</sup> and other junction-based photovoltaic devices.<sup>42–45</sup> One should note that a relatively low FF is not inherently related to *p*DSCs (or NiO), but its value is rather ruled by the built-in potential of the device, i.e. by the redox potential of the mediator and the structure of the VB in the semiconductor. At this regard there are four main factors to consider: (i) the generally slower mobility and smaller rate of photoinjection of the holes in *p*-type photocathodes when compared to electrons in *n*-type photoanodes;<sup>46</sup> (ii) phenomena of optical self-absorption in defective *p*-type oxides like non-stoichiometric NiO<sub>x</sub> [in this case the Ni(III) sites, i.e. the hole-carriers, represent formally the colour centres],<sup>37</sup> which unavoidably limit the thickness (*l*) that leads to the attainment of a mesoporous transparent photocathode and, consequently, the extent of dye-loading; (iii) the occurrence of recombination processes between iodide anions and the photo-injected holes that transit in proximity of the cathode/electrolyte interface;<sup>47,48</sup> (iv) capacitive properties of *p*-type NiO itself.<sup>49</sup> At this regard two different approaches have been adopted to solve these issues: (a) amelioration of both electronic and morphologic properties of the photocathode;<sup>50</sup> (b) passivation of the electrode surface by thermal treatment<sup>51</sup> or via addition of a surface modifier with no redox activity and/or light absorption properties.<sup>30,52–54</sup> For the last approach it has been found that the thermal treatment has the advantage of increasing the optical transparency of the NiO film, but it also brings about a significant diminution of the number of surface sites for dye-anchoring.<sup>51,55</sup> An efficacious way of passivating the surface of NiO is the addition of CDCA either in the electrolyte of the *p*-DSC,<sup>30</sup> or in the dyeing solution of NiO.<sup>57</sup> This is because CDCA reacts with the Ni(III) centres and renders them totally inactive towards recombination.<sup>56</sup> On the other hand, the use of CDCA has a drawback: the surface passivation of NiO with CDCA consists in a phenomenon of chemisorption that “blinds” the Ni(III) sites of dye-anchoring.<sup>58</sup> Such sites are no longer available to the colorant for the further sensitization of the electrode. On the other hand, if blocking layers<sup>59,60</sup> or electronically insulating materials in the nanoparticulate form<sup>61</sup> are in direct contact with the dye-sensitized *p*SC there is still the inhibition of undesired phenomena of recombination at the dye-*p*SC/electrolyte interface. A consequence of the presence of extraneous insulating species within the SC is the prevention of intermolecular dye aggregation onto the sensitized surface of *p*SC (similarly to what CDCA effectuates). For the controlled passivation of sensitized NiO cathodes against photohole recombination in operating *p*-DSCs, the inclusion of ZrO<sub>2</sub> NPs in thin films of nanostructured NiO was considered.<sup>61</sup> The choice of screen-printed NiO/ZrO<sub>2</sub> nanocomposites as cathodic substrates of *p*-DSCs led to the realization of *p*-type devices with overall photoconversion efficiencies that were almost 50 % higher than the typical efficiency of a *p*-DSC with sole nanostructured NiO as cathodic material.<sup>61</sup> This finding was accompanied by the increase of electron transfer resistance through the photocathode/electrolyte interface in passing from sole NiO to the nanocomposite NiO/ZrO<sub>2</sub> cathode.<sup>61</sup> It was concluded that ZrO<sub>2</sub> islands in screen-printed NZNC decreased efficaciously the probability of recombination between surface-trapped holes (injected in NiO) and the photoreduction product I<sup>-</sup> at the NZNC photocathode/electrolyte interface because of the diminution of the effective contact area between exposed NiO and the electrolyte while the kinetics of holes photoinjection in NZNCs was practically unaffected by ZrO<sub>2</sub> addition within certain limits of compositions. In the present work we have considered the production and the characterization of *p*- and *t*-DSCs with NZNCs as cathodic materials and P1<sup>62–65</sup> as dye-sensitizer when NZNCs are deposited in the configuration of thin films ( $l < 3 \mu\text{m}$ ) via spray deposition (SD) of NiO/ZrO<sub>2</sub> NPs suspensions and successive sintering in conventional oven [at temperatures below 500 °C (*vide infra*)]. SD was chosen because it has the advantages of producing in an easy, safe and reproducible way mixed-oxides films the thickness and composition of which can be modulated by varying

the number of spraying passes and the concentration of oxide NPs in the sprayed suspension (*vide infra*). ZrO<sub>2</sub> (a ceramic material) has been chosen as “diluting agent” of the surface defects (i.e. the recombination centres) of NiO since it constitutes a redox-inactive metal oxide with chemical inertness and long-term chemical-physical stability.<sup>66</sup>

The NZNCs under consideration are actually solid solutions of NiO and ZrO<sub>2</sub> nanodomains.<sup>61,67</sup> This is because the nanocomposite mixed oxide does not present a characteristic crystal and electronic structure of its own when NiO/ZrO<sub>2</sub> molar ratio is higher than 8. In fact, the XRD patterns of the NZNCs are equivalent to the sum of the diffraction spectra of the separated parent precursors NiO and ZrO<sub>2</sub> in the nanostructured version when NiO and ZrO<sub>2</sub> have comparable concentration in the composite.<sup>68</sup> It will be shown that P1-sensitized NZNCs thin films can produce *p*-DSCs with overall efficiencies as high as 0.16 % when I<sup>-</sup>/I<sub>3</sub><sup>-</sup> is the redox shuttle. Such an improvement of the photoconversion performance will be ascribed to the combined effect of two concomitant causes: i) increase of the recombination resistance at the NZNC/electrolyte interface of the *p*-DSC; ii) an increase of the overall electrical conductivity of NZNCs with respect to the electrode of sole NiO. At the synthetic level the adoption of SD as deposition method of nanostructured NZNCs affords samples with higher porosity and, consequently, higher dye-loading in comparison to the analogous nanocomposites deposited via screen-printing.<sup>61</sup> This will have favourable consequences on the photoconversion properties of the corresponding *p*-type cells. The use of spray-deposited nanostructured NiO/ZrO<sub>2</sub> composites as photocathodic material was extended also to tandem DSCs (*t*-DSCs) when sensitized titania (TiO<sub>2</sub>) was the photoanode. We report here the attainment of the maximum value of 1.88% for the overall efficiency of the *t*-DSC that employs VG10-C8 squaraine<sup>69</sup> and P1 as anode and cathode sensitizers, respectively. To our knowledge, this represents the highest value ever reported for a tandem device in which both photoanode and photocathode have comparable kinetics of carriers photoinjection.

## Experimental

NiO NPs with average diameter ( $\phi$ ) of 35 nm, CDCA, isopropanol, methanol, acetone, anhydrous acetonitrile and absolute ethanol were purchased from Sigma Aldrich at the highest degree of purity and employed without any further purification. ZrO<sub>2</sub> NPs ( $\phi$  = 20 nm) were purchased from US Research Nanomaterials. FTO/glass substrates (TEC7) was from NSG. P1 was purchased from Dyenamo. VG10-C8 was synthesized as previously reported by some of us<sup>70</sup>.

In the SD method,<sup>71</sup> the dispersion to be sprayed had the mass concentration of 10 mg of NiO NPs precursor per mL of methanol (solvent). Dispersion was sprayed with a constant flow rate of 30  $\mu\text{L min}^{-1}$  at 0.55 mPa of operating pressure with nitrogen gas as atomizer. The nozzle position was controlled along two coordinates through a home-made software in order to define the deposition area. The scan rate of the nozzle was set at 10 mm s<sup>-1</sup> while the distance between the nozzle and the substrate was 15 mm. The number of passes (i.e. the repetition of a single SD procedure on the same area) was fixed at 4. During deposition, the substrate was heated up and its temperature was maintained at 70 °C. Six different dispersions of the metal oxides NPS in methanol were considered for SD. The methanol dispersions had a total volume of 20 mL and varied for the values of ZrO<sub>2</sub>/NiO molar ratio. In every dispersion the mass of NiO NPs was constant and set at 200 mg with resulting mass concentration of 10 mg mL<sup>-1</sup>. The mass of ZrO<sub>2</sub> NPs was varied in the different dispersion in order to obtain the following ZrO<sub>2</sub>/NiO molar ratio values:

- NiO benchmark, no ZrO<sub>2</sub>
- ZrO<sub>2</sub>/NiO = 0.01, with 3.3 mg of ZrO<sub>2</sub>

- $\text{ZrO}_2/\text{NiO} = 0.02$ , with 6.6 mg of  $\text{ZrO}_2$
- $\text{ZrO}_2/\text{NiO} = 0.05$ , with 16.5 mg of  $\text{ZrO}_2$
- $\text{ZrO}_2/\text{NiO} = 0.10$ , with 33.0 mg of  $\text{ZrO}_2$
- $\text{ZrO}_2/\text{NiO} = 0.20$ , with 66.0 mg of  $\text{ZrO}_2$

The spray-deposited samples were named  $\text{NiO-ZrO}_2\text{-X}$  with X indicating the molar ratio  $\text{ZrO}_2/\text{NiO}$ . All the dispersions were chemically and physically stable up to 15 days of storage in ambient conditions. Before spraying, the precursor dispersion underwent ultrasonic agitation for 30 minutes to obtain a homogenous suspension- The latter was successively sprayed onto an FTO/glass substrate. The glass substrate had  $l = 2.2$  mm. Prior to SD the FTO/glass substrate was previously cleaned through ultrasonic agitation in both acetone and isopropanol. Duration of ultrasonic cleaning was 30 minutes in each solvent. The FTO plate was scotch-taped to obtain an active area of  $0.5 \times 0.5 \text{ cm}^2$ . The as-deposited electrodes were sintered for 30 minutes in oven at  $450^\circ\text{C}$ .<sup>72</sup>

Thickness measurements were made through an optical profilometer (Dektak 150<sup>®</sup> from Veeco). FESEM Auriga Zeiss Field Emission was employed to investigate the morphology of the electrodes. Energy Dispersive X-ray Spectroscopy (EDX Quantax Bruker, Resolution 123 eV ( $\text{Cu K}\alpha$ )) was used for the elemental analyses. The DaVinci D8 diffractometer, equipped with a  $\text{Mn K}\alpha$  as exciting source, was used for the determination of the XRD spectra of the SD nanocomposites.

To perform X-ray Photoelectron Spectroscopy (XPS)  $\text{NiO/ZrO}_2$  samples were mounted onto the sample holder with an adhesive scotch tape and electrically contacted with a drop of silver paste bridging the conducting top layer of the glass to the stainless-steel holder. XPS measurements were performed with a modified Omicron NanoTechnology MXPS system equipped with a monochromatic X-ray anode (Omicron XM-1000) and an Omicron EA-127 7-channeltron energy analyser. XP spectra were acquired using  $\text{Al K}\alpha$  photons ( $h\nu = 1486.7 \text{ eV}$ ) as excitation source, generated with the anode operating at 14 kV and 16 mA. No charging was experienced during measurements. For all the samples the spectral regions associated with the ionization of Ni 2p, Zr 3d, O 1s, C 1s levels were acquired using an analyser pass energy of 20 eV. A survey scan at 50 eV of pass energy was also recorded. A take-off angle ( $\theta$ ) of  $21^\circ$  with respect to the direction normal to the surface was used. The measurements were performed at room temperature and the base pressure in the analyser chamber was about  $2 \times 10^{-9}$  mbar during the recording of the spectra. XPS Zr/Ni atomic ratios were estimated from experimentally determined area ratios (with  $\pm 10\%$  as associated error), which were corrected for the corresponding photoelectron cross-sections according to Scofield calculations,<sup>73</sup> and for the square root dependence of the photoelectrons kinetic energy. Optical transmittance of NZNC electrodes was measured with a double-ray spectrometer [UV-2550 by Shimadzu, Kyoto (JP)], using air as reference and operating in direct mode.

The photocathodes were sensitized by dipping in an ACN solution of P1 dye.<sup>74</sup> The *p*-type devices were made by coupling the SD photocathode with a counter-electrode (CE) based on Pt NPs.<sup>75</sup> A thermoplastic resin (Surlyn<sup>®</sup>, from Dupont), was used as spacer and sealant. Electrolyte (H from Dyesol<sup>®</sup>) was injected in the cell by back-vacuum filling technique. For the assembly of *t*-DSCs, the Pt-based CE was replaced by an 8  $\mu\text{m}$ -thick  $\text{TiO}_2$  photoanode. The sensitization of the latter was performed by dipping the photoanode in an ethanol solution of VG10-C8<sup>70</sup> (Figure 1) and CDCA<sup>76</sup> in the concentration ratio 1/10. Before photoelectrochemical characterization all DSCs were kept in the dark for 24 hours.

The photoelectrochemical characterization of the *p*-DSCs consisted in the recording of the *JV* characteristic curves and incident photon-to-current conversion efficiency (IPCE) spectra. All the measurements were recorded under 1 sun light intensity ( $100 \text{ mW cm}^{-2}$ , AM 1.5G) provided by an AAA class sun simulator equipped with a 150 W xenon arc lamp (91195A, Newport Corp., Irvine, CA, USA) and connected to a digital source meter (2420, Keithley Instrument Inc., Cleveland, OH, USA), after calibration with a silicon reference solar cell (91150V, Newport Corp.). The curves of IPCE were recorded using a computer-controlled set-up consisting of a Xe lamp (Mod.70612, Newport) coupled to a monochromator (Cornerstone 130 from Newport), and a Keithley 200 2420 light-source meter. Electrochemical Impedance Spectroscopy measurements were performed with an AUTOLAB PGSTAT12® from Metrohm remotely controlled by NOVA software at the condition of open circuit (with a potential perturbation had an amplitude of 20 mV) under solar simulator illumination within a frequency range of  $10^{-2}$ – $10^5$  Hz. EIS spectra were fitted using Z-View software from Scribner Associates Inc. taking advantages of custom-developed equivalent circuits.

## Results and discussion

**Physical properties of NZNCs.** All investigated SD nanocomposite electrodes of NZNC presented a mesoporous open morphology as fundamental requirement for an efficacious dye-loading (Figure S1). The addition of  $\text{ZrO}_2$  NPs in the range of molar concentration here considered did not lead to a significant alteration of the roughness and the morphology of the NZNC electrodes with respect to sole NiO films (top left image in Figure S1). The EDX images of the NZNC electrodes (Figure 1) reveal that the superficial atomic ratio Ni/Zr is generally lower than the nominal value derived from the relative concentrations of NPs precursors in the preparative solution (as also proved by XPS analyses, vide infra). This leads us to conclude that  $\text{ZrO}_2$  NPs are preferentially localized onto the surface of the NZNC films rather than in the bulk if the composition of the preparative solution is retained also in the corresponding NZNC.

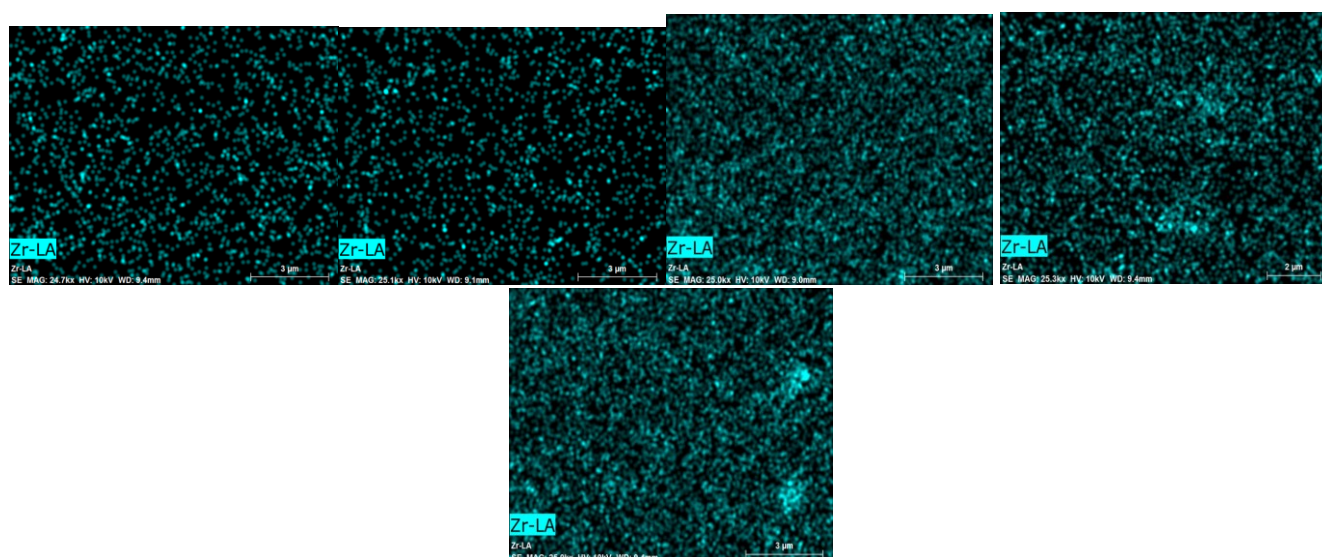


**Figure 1.** EDX images of the different  $\text{NiO\_ZrO}_2\text{-X}$  electrodes prepared via SD. The cyan coloured areas indicate the zones of the NZNC surfaces where Zr is present. Top left: image of the NZNC with Zr/Ni ratio 1%; top right: Zr/Ni = 2%; middle left: Zr/Ni = 5%; middle right: Zr/Ni = 10%; bottom: Zr/Ni = 20%.

Table 1 reports the elemental composition (as obtained by the analysis with SEM-EDX or XPS facility) for each type of NZNC electrode and the corresponding roughness. The first column from right in Table 1 reports the analogous data of the NiO electrode obtained via screen-printing<sup>53</sup> for sake of comparison with the data of SD NiO (second column from left).

The EDX images of the different NZNC electrodes show the localized presence of Zr through the colored areas (Figure 1). Reasonably, the EDX signal of Zr atoms increases in passing from lower to higher Zr/Ni ratio. The dispersion of ZrO<sub>2</sub> NPs results quite uniform on the surface of the nanocomposite surface when Zr/Ni < 10 %. Only at larger concentrations of ZrO<sub>2</sub> in the starting dispersion (Zr/Ni ≥ 10%) there is the verification of ZrO<sub>2</sub> macrostructures formation (Figure 1, middle and bottom pictures). From the general analysis of the morphologies and the patterns of surface distribution of the metallic atoms for the different NZNC samples it results clear that SD affords a very homogeneous dispersion of ZrO<sub>2</sub> NPs in the matrix of nanostructured NiO. If compared to screen-printing, SD results a better deposition method in terms of homogeneity of NP dispersibility since screen-printed NZNC films show ZrO<sub>2</sub> macrostructures already at Zr/Ni molar ratio values of *ca.* 5 %.<sup>61</sup>

**Table 1.** Atomic content (in percentage) as evaluated from the EDX measurements on SD-electrodes when the content of ZrO<sub>2</sub> varied in the starting suspension. The first column on the right reports the compositional analysis of screen-printed NiO when this was deposited onto FTO

Atomic content / %	SD NiO	NiO_ZrO <sub>2</sub> 0.010	NiO_ZrO <sub>2</sub> 0.020	NiO_ZrO <sub>2</sub> 0.050	NiO_ZrO <sub>2</sub> 0.100	NiO_ZrO <sub>2</sub> 0.200	Screen- printed NiO
O	56.3	56.8	55.9	57.4	57.1	57.3	57.5
Ni	37.3	36.8	34.9	34.5	32.4	29.8	37.1
Zr	-	0.6	1.0	2.0	3.6	6.2	-
Sn	-	-	-	-	-	-	0.9
C	6.3	5.8	8.2	6.1	6.9	6.7	4.5
ZrO <sub>2</sub> /NiO (by EDX)	-	1.6	2.7	5.9	11.0	20.9	-
ZrO <sub>2</sub> /NiO (by XPS)	-	-	3.4	7.2	-	-	-
Ni/O	66	65	63	60	57	52	64

Moreover, the SD samples do not show the signal of Sn (from underlying FTO) in the EDX images. This implies that the coverage of the transparent conductive substrate through the SD procedure is much more uniform than in case of the coatings obtained via screen-printed NZNCs.<sup>61</sup> The presence of ZrO<sub>2</sub> on the surface of pristine NZNC does not bring about a sizeable diminution of dye-loading at low levels of ZrO<sub>2</sub> addition when Zr/Ni ≤ 0.05 (*vide infra* Table 2, first column on the right). This indicates that low levels of ZrO<sub>2</sub> do not alter the reactivity of NiO towards a given sensitizer, i.e. under these conditions ZrO<sub>2</sub> does not practically dilute the surface concentration of defective Ni(III) sites<sup>77</sup> in correspondence of which dye-anchoring is supposed to occur.<sup>33,58</sup> The further increase of Zr content in NZNC films (when Zr/Ni > 0.05) leads to the formation of ZrO<sub>2</sub> macrostructures in association with the decrease of dye-loading capability (*vide infra* Table 2, first column on the right).

In Figure 2 the films of SD NZNCs presented a diffraction pattern that did not significantly vary with the increase of ZrO<sub>2</sub> content and reproduced the one of sole NiO in the nanostructured version (JCPDS card No. #47-1049). Peaks at 11.82°, 15.04°, 22.78° and 23.01° are due to the FTO layer whereas the peak at 27.00° is ascribable to the NiO substrate.<sup>61</sup>



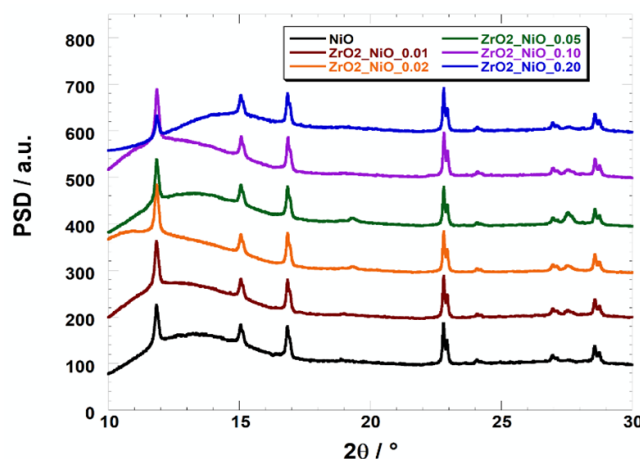


**Figure 2.** XRD spectra of the SD nanocomposites of NiO and ZrO<sub>2</sub> differing for the chemical composition. The pattern of diffraction of the film of sole nanostructured NiO on the same substrate of FTO/glass is reported as internal reference.

As far as the photoactive film is concerned, the signals at 16.83° and 28.60° (partially split) are due to plane (111) and (220) of NiO, respectively. The peak at 27.57° varied with the amount of ZrO<sub>2</sub> in the nanocomposite film (Figure 2). This is not present in the diffractogram of sole nanostructured NiO and it systematically raises with the amount of dopant. This was straightforwardly ascribed to the plane (311) of tetragonal ZrO<sub>2</sub> (JCPDS card No. #79-1769).<sup>68</sup> When the concentration of ZrO<sub>2</sub> dopant is higher than 10% the intensity of ZrO<sub>2</sub> plane (311) tends to decrease and the signal becomes broader. This is probably due the onset of the formation of ZrO<sub>2</sub> micro-islands that possess prevalently an amorphous structure rather than a crystalline one. The absence of NZNCs specific diffraction peaks in the spectra of the nanocomposites as well as the quasi constancy of the relative intensities of the diffraction peaks of NiO in these, denote the lack of formation of a new mixed oxide of the type Ni<sub>x</sub>Zr<sub>y</sub>O with its own specific crystal structure.

To further confirm the absence of new mixed oxides and to get more insight in the charge state of the spray-deposited electrodes, we performed XPS analyses on selected samples. Figure 3 shows the  $j = 3/2$  portion of the Ni 2p region of the NiO, NiO\_ZrO<sub>2</sub>\_0.02, and NiO\_ZrO<sub>2</sub>\_0.05 samples. The Ni 2p lineshape is complicated by the several final-state components typical of NiO, as already reported by us and other authors.<sup>23,78</sup> These components are here simplified by lines, from A to F, indicating their relative position and intensity. The most intense peak (A) is attributed to the  $cd^9L$  state (with c and L respectively representing holes in the 2p level and in a ligand orbital),<sup>79,80</sup> while B and C peaks are associated to non-local core-hole screening processes and charge transfers at low-coordinated Ni centres mostly located at the surface.<sup>81,82</sup> Peaks D, E and F are respectively associated to  $cd^{10}L^2$  and  $cd^8$  final states, and a shake-up transition.<sup>78,83</sup> As it turns out from the spectra in Figure 3, all three samples look very similar, with no sizeable effect resulting from the presence of ZrO<sub>2</sub>.

Even if NiO generally contains Ni<sup>3+</sup> defects, their recognition within the Ni 2p photoionization spectrum has been widely acknowledged to be a complicated task, since the main Ni<sup>3+</sup> feature falling in the B peak region results substantially shadowed by the Ni<sup>2+</sup> *non-local screening* processes.<sup>83,84</sup> A more straightforward detection of Ni<sup>3+</sup> species has been proposed in genuine Ni(III) compounds, such as in the case of NiOOH polymorphs<sup>23,78</sup> and spinel-type nickel cobaltites<sup>85</sup>.

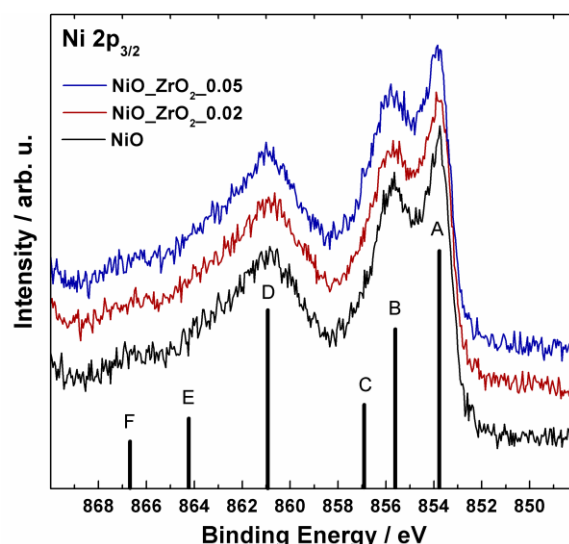


**Figure 3.** Ni2p<sub>3/2</sub> photoionization region of three relevant samples: reference NiO (black), NiO\_ZrO<sub>2</sub>\_0.02 (red), and NiO\_ZrO<sub>2</sub>\_0.05 (blue). Bars with capital letters indicate position and relative intensity of final-states in photoionised NiO according to ref <sup>23</sup>.

The close similarity among the Ni 2p spectra in Figure 3 suggests that the possible presence of very dilute Ni<sup>3+</sup> defects and their interaction with ZrO<sub>2</sub> could not be detected through XPS.<sup>86</sup>

Figure S2 shows the Zr 3d photoionization region, composed by a spin-orbit split ( $j'' = 5/2$  and  $j' = 3/2$ ) doublet with components at 182.3 and 184.7 eV, fully consistent with already reported data on ZrO<sub>2</sub>.<sup>87</sup> In particular, the binding energy position of Zr 3d doublet is not affected by electrostatic charging due to poor conductivity, confirming that ZrO<sub>2</sub> is present as relatively small nanostructures.<sup>87</sup> The Zr/Ni atomic ratio has been determined on the two samples analysed with XPS, resulting in 3.4% and 7.2%, respectively for NiO\_ZrO<sub>2</sub>\_0.02, and NiO\_ZrO<sub>2</sub>\_0.05 samples. Therefore, the Zr content, as determined by XPS, results slightly higher than its nominal value, probably due to a partial enrichment at the surface of the film.

Similar to screen-printed NZNCs,<sup>61</sup> also the SD samples of NZNCs can be considered solid solutions of ZrO<sub>2</sub> nanodomains (of variable extent) that are embedded into a matrix of nanostructured NiO. The XRD peaks characteristic of ZrO<sub>2</sub> domains are barely detectable for the low amount in thin film samples. Inclusion of ZrO<sub>2</sub> in the NiO matrix does not affect the optical properties of the resulting SD nanocomposite thin films as verified by the comparison of the transmittance spectra for the various NZNCs (Figure 4).

**Characterization of DSCs.** The *p*-DSCs here characterized have been assembled with P1-sensitized NZNCs as photocathodes while the anode was constituted by FTO embedded with Pt-NPs. P1 dye (Figure S3) is a sensitizer designed specifically for achieving efficient *p*-DSCs with NiO cathodes.<sup>65</sup> Five different devices with same nominal characteristics were tested to check the reproducibility of device performance. The *JV* curves of the different NiO\_ZrO<sub>2</sub>\_X based cells are reported in Figure 5. The corresponding photoelectrochemical parameters are reported in Table 2.

Ongoing from bare nanostructured NiO to the nanocomposite NiO\_ZrO<sub>2</sub>\_0.05 as cathodic material, it is observed an increase in the efficiency of the corresponding *p*-DSCs (Table 2, second column from left). Within the compositional range 0-0.05 the presence of ZrO<sub>2</sub> nanodomains is then beneficial and does not practically affect the parameter of dye-loading since the latter varies in the narrow interval  $3.7\text{-}3.8 \times 10^{-8} \text{ mol cm}^{-2}$  (Table 2, first column from left). Both overall efficiency ( $\eta$ ) and short-circuit

current density ( $J_{sc}$ ) increase with the amount of  $ZrO_2$  in the nanocomposite photoelectrodes when the content of  $ZrO_2$  is not larger than 5% in the nanocomposite. An increase of the  $J_{sc}$  parameter implies that the addition of  $ZrO_2$  NPs in nanostructured NiO varies necessarily (and favourably) at least one of the following three factors at the microscopic level with respect to sole nanostructured NiO: (i) the number of charge carriers (by enlarging it); (ii) the rate of injection of the charge carriers (by augmenting it); (iii) the mobility of the photoinjected charge carriers through the electrode (by increasing it).

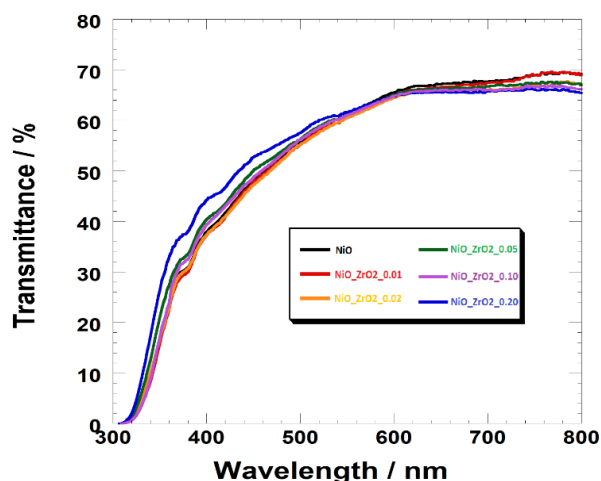


**Figure 4.** Optical transmittance spectra of the different  $ZrO_2$ /NiO nanocomposites prepared via spray deposition

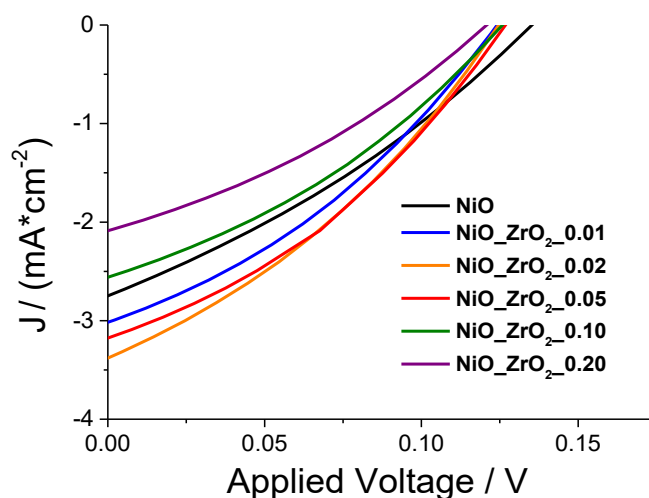


**Figure 5.** JV characteristic curves of the  $p$ -DSCs differing for the chemical composition of the NZNC cathode

**Table 2.** Photoelectrochemical parameters of the  $p$ -DSCs employing nanocomposite SD NiO\_  $ZrO_2$ \_X electrodes as cathodes. Parameters have been extracted from the JV curves shown in Figure 5. The parameters of the most performing device are reported in brackets for the different compositions of the nanocomposite cathodes.

Photocathode	$V_{oc}$ / mV	$J_{sc}$ / $mA\ cm^{-2}$	FF / %	$\eta$ / %	Dye-loading / $10^{-8}\ mol\ cm^{-2}$
NiO	$127 \pm 2$ (128)	$-2.73 \pm 0.14$ (2.84)	$33.2 \pm 0.7$ (33.5)	$0.115 \pm 0.008$ (0.122)	3.7
NiO_ $ZrO_2$ _0.01	$126 \pm 3$ (128)	$-2.98 \pm 0.16$ (3.16)	$34.2 \pm 0.7$ (34.5)	$0.128 \pm 0.012$ (0.139)	3.8
NiO_ $ZrO_2$ _0.02	$124 \pm 1$ (126)	$-3.39 \pm 0.21$ (3.65)	$34.5 \pm 0.6$ (35.2)	$0.146 \pm 0.014$ (0.162)	3.8
NiO_ $ZrO_2$ _0.05	$126 \pm 2$ (127)	$-3.12 \pm 0.23$ (3.42)	$34.8 \pm 0.5$ (35.3)	$0.137 \pm 0.011$ (0.153)	3.7
NiO_ $ZrO_2$ _0.10	$123 \pm 1$	$-2.47 \pm 0.170$	$33.7 \pm 0.8$	$0.103 \pm 0.005$	3.1

	(124)	(2.62)	(34.7)	(0.113)	
<b>NiO_ZrO<sub>2</sub>_0.20</b>	121 ± 1 (121)	-2.10 ± 0.27 (2.30)	34.3 ± 1.0 (34.7)	0.087 ± 0.021 (0.096)	2.5
<b>screen-printed NiO</b>	129 ± 2 (130)	-1.45 ± 0.12 (-1.50)	32.5 ± 0.6 (32.9)	0.060 ± 0.011 (0.065)	3.2

The inhibition of recombination phenomena (as verified through EIS) might influence at a different extent all three factors listed here. If recombination is inhibited by ZrO<sub>2</sub> NPs prevalently in correspondence of the electrode/electrolyte interface, i.e. the zone of charge carrier photogeneration, a favourable effect also on  $V_{OC}$  and FF would be observed provided that recombination inhibition ameliorates (i) and (ii). On the other hand, recombination inhibition would not considerably affect the values of  $V_{OC}$  and FF if recombination affects charge carrier mobility (iii). The combination of the observations reported here leads us to suppose that at the microscopic level the presence of ZrO<sub>2</sub> NPs produces its beneficial effects on the overall performance of the DSCs mostly at the bulk level of the cathode rather than at the interfacial level.

The favourable influence little fractions of ZrO<sub>2</sub> exert in the photocathode performance is ascribed to the abatement of the recombination interfacial phenomena by virtue of ZrO<sub>2</sub> redox inactivity. This feature of ZrO<sub>2</sub> has a favourable influence on the charge transport properties of the NZNC cathode since the inhibition of recombination at the electrode surface allows the injection of a larger amount of mobile charge carriers in the NZNC. The recombination consists in the redox reaction between I<sup>-</sup> anions and Ni(III) sites with the latter representing the chemical species corresponding to the photoinjected holes.<sup>88</sup>

The effect of ZrO<sub>2</sub> concentration on both the charge transport and recombination in NZNC electrodes have been deeply investigated in a previous paper by some of us.<sup>61</sup> Albeit the deposition technique is different, similar behaviour could be fairly expected because the deposition method greatly influences the morphology of the electrode, but it is less impacting on the chemistry of the system. To further confirm this, we performed some EIS analyses on selected sample and we compared them with the results obtained in ref <sup>61</sup>. As one can see from table S1, in both cases the electrode containing 2% of ZrO<sub>2</sub> showed lower charge transport resistance and higher charge recombination resistance. This results in a longer hole diffusion length ( $L_h$ ) and, thus, better photovoltaic properties (vide infra). The parameters of  $J_{sc}$  and  $\eta$  increase quasi linearly with ZrO<sub>2</sub> ongoing from the *p*-DSC with sole NiO cathode (-2.733 mA cm<sup>-2</sup> and 0.115%) to the most performing electrode NiO\_ZrO<sub>2</sub>\_0.02 (-3.388 mA cm<sup>-2</sup> and 0.146 %). The values of the open circuit photopotential  $V_{oc}$  in the tested *p*-DSCs are practically invariant with the content of ZrO<sub>2</sub> in the nanocomposite electrode (Table 2, second column from left) when ZrO<sub>2</sub> is less than 5%. The parameter of  $V_{oc}$  is controlled by the efficiency of carrier photogeneration and the lifetime of the photoinjected charges.<sup>89</sup> Charge lifetime is, in turn, dependent on the rate of interfacial recombination when no electrical current is traversing the electrode. Such a lack of the dependency of  $V_{oc}$  on ZrO<sub>2</sub> content indicates that the redox-inactive oxide does not shorten photocarrier lifetime in absence of the passage of current. In this context, ZrO<sub>2</sub> manifests its beneficial role of recombination inhibitor under dynamic conditions, i.e. when the photoinjected charges traverse the electrode and continuous replenishment of I<sub>3</sub><sup>-</sup> (by diffusion from the electrolyte) is involved at the electrode/electrolyte interface. The fill factor FF (Table 2, third column from right) increases from 33% in the *p*-DSC with NiO photocathode to 35% in the cells with NiO\_ZrO<sub>2</sub>\_0.05 photocathode.

For the realization of the best performing *p*-DSCs with NZNC electrodes, the optimal composition of the nanocomposite cathode is  $X = 0.02$ . In the compositional range  $0.02 < X \leq 0.05$   $J_{sc}$  and  $\eta$  diminish progressively with  $X$  but the photoconversion performance of the corresponding cells is still better than the one of the *p*-DSCs with SD NiO ( $X = 0$ ). Upon further increase of

the ZrO<sub>2</sub> content ( $X > 0.1$ ) in the NZNC cathodes the photoconversion properties of the *p*-type cells deteriorate also in comparison to the *p*-DSC with SD NiO.

This was mainly ascribed to the appearance of ZrO<sub>2</sub> macrostructures (Figure 2, bottom image) that reduce dye-loading on the surface of NiO (-17% and -32% for NiO\_ZrO<sub>2</sub>\_0.10 and NiO\_ZrO<sub>2</sub>\_0.20, respectively). This consequently limits the photocurrent in the corresponding devices. As observed before, the best performing photoelectrochemical cell was the *p*-DSC with P1-sensitized NiO\_ZrO<sub>2</sub>\_0.02 photocathode ( $V_{oc} = 126$  mV,  $FF = 35.2\%$ ,  $J_{sc} = 3.652$  mA cm<sup>-2</sup> and  $\eta \approx 0.16\%$ ). The trend of the photoconversion efficiency of the cells employing SD photocathodes retraces the one previously found with the *p*-DSCs having screen-printed photocathodes.<sup>61</sup> Such a parallel photoelectrochemical behaviour of the ZrO<sub>2</sub>-containing cathodes prepared with different deposition methods shows that ZrO<sub>2</sub> has the same type of influence in the NZNCs regardless of the preparation method.

The optimum photocathode SD NiO\_ZrO<sub>2</sub>\_0.02 of the most performing *p*-DSC was also used in a tandem device. P1-sensitized NiO\_ZrO<sub>2</sub>\_0.02 was combined with a photoanode of dye-sensitized nanostructured TiO<sub>2</sub> (thickness: 8 μm; sensitizer: blue VG10-C8 squaraine, Figure S3). For the definition of the photoanode in the *t*-DSC we have chosen a value of TiO<sub>2</sub> thickness and a sensitizer that produce in the corresponding *n*-DSC (i.e. in the device with the sole anode as photoactive electrode) photocurrent values in the order of 3 mA cm<sup>-2</sup>, i.e. the maximum value achievable with SD NZNC based *p*-DSC (Table 2, third column from left). In doing so, we aim to achieve current matching in the tandem device. VG10-C8 squaraine (Figure S4) was chosen as anodic colorant because its absorption spectrum is complementary to that of P1 (Figure S4). In the assembly of the tandem device the thickness of nanostructured TiO<sub>2</sub> photoanode was adjusted in a way that VG10-C8 sensitized TiO<sub>2</sub> would produce a photocurrent density as close as possible to 3.5 mA cm<sup>-2</sup> in the *n*-DSC. As observed before, the value of 3.5 mA cm<sup>-2</sup> corresponds to the maximum photocurrent density achievable with a *p*-DSC employing the SD P1-sensitized NZNC photocathode when  $X = 0.02$ . The matching of the currents produced by the two DSCs with single photoactive electrode allows the assembly of the corresponding *t*-DSC with *JV* curves that do not present a S-shaped profile (Figure 6, top frame). The external quantum efficiency IPCE spectra of *p*-, *n*- and *t*-DSC (with the latter illuminated from photocathode side) are reported in Figure 6 (bottom frame). The corresponding photoelectrochemical parameters extrapolated from the data of Figure 6 are summarized in Table 3. The IPCE spectrum of the *t*-DSC is very similar to the one of the *p*-type device in terms of both shape and intensity within the spectral region 300-600 nm since the tandem cell was irradiated from the photocathode.

When compared to the one of the parent *n*-DSC, the IPCE profile of the *t*-DSC (Figure 6, bottom frame, blue profile) shows a uniform diminution of efficiency (*ca.* 10%, on average) in the spectral range where VG10-C8 sensitized-TiO<sub>2</sub> exerts its photoelectrocatalytic action (interval:  $540 < \lambda < 800$  nm). This is because the photoanode contribution in the IPCE spectrum of the *t*-DSC is practically null in the range 300-600 nm when the *t*-DSC is illuminated from the photocathode. In these operative conditions the radiation results completely absorbed by the sensitized photocathode and in part also by the iodide-based electrolyte. The contribution of the photoanode in the IPCE spectrum of the tandem cell becomes evident at higher wavelengths ( $\lambda > 580$  nm) but is lower within the same spectral range if compared to the *n*-type device with same photoanode because of the non negligible absorption of the various layers in front of TiO<sub>2</sub>-based anode. When opposite geometry is tested (i.e. device illuminated from the photoanode) a different spectrum is recorded; in this case, the photocathode seems to not sizeably contribute to the IPCE (Figure S5). This is mainly due to the parasitic absorption of the iodine-based electrolyte that partially filter the radiation before it could reach the photocathode.

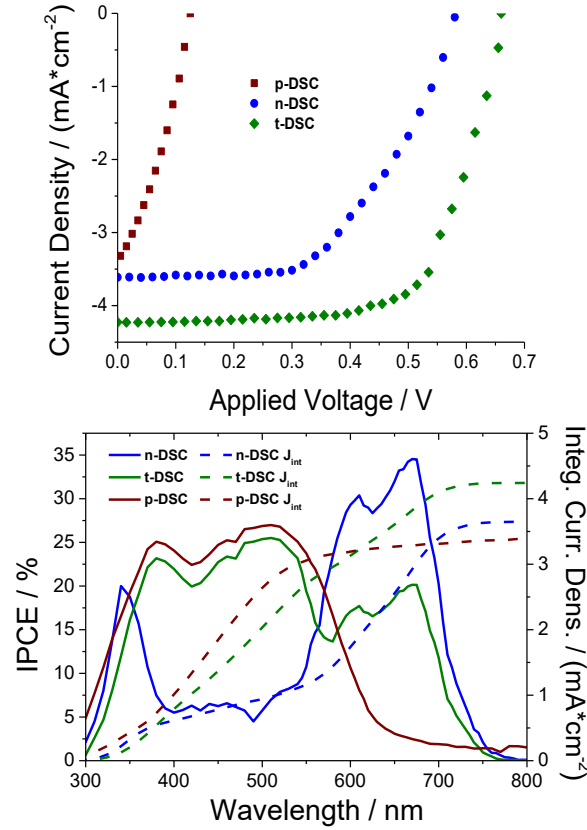


**Figure 6.** (Left) JV and (right) IPCE profiles of (blue) *n*-DSC, (brown) *p*-DSC and (green) *t*-DSC when the NZNC cathode with  $X = 0.2$  is sensitized with P1 and the  $\text{TiO}_2$  anode is sensitized with VG10-C8. Dotted lines in the right frame refer to the  $J_{sc}$  integrated curve recorded during the collection of the IPCE spectra. The *t*-DSC was illuminated from the side of the photocathode.

Additionally, the spectrum in the NIR region is lower compared to the one of single-junction *n*-DSC due to the fact the NZNC photoelectrode is not able to support the same current supported by a photoinactive Pt-based device. The *n*-DSC (*p*-DSC) powered a photocurrent density of 3.6 (3.3)  $\text{mA cm}^{-2}$  with open circuit voltage of 580 (120) mV and FF of 0.68 (0.34). These parameters led to overall photoconversion efficiencies of 1.43% and 0.15% for the *n*-DSC and *p*-DSC, respectively. The *t*-DSC displayed better photoconversion properties in comparison to the parent *n*- and *p*-DSCs. This is obvious for the parameter of the open circuit voltage<sup>16</sup> ( $V_{oc} = 680$  mV in *t*-DSC, Table 3). The OCV value of 680 mV is the result of the difference between the upper edge of the valence band of the *p*-type semiconductor ( $\text{ZrO}_2/\text{NiO}$  nanocomposite) and the lower edge of the conduction band of the *n*-type semiconductor ( $\text{TiO}_2$ ). The most interesting aspect is represented by the trend of the short-circuit current density since *t*-DSC with  $J_{sc} = 4.2$   $\text{mA cm}^{-2}$ , displays the higher value in comparison to the ones photogenerated by the cells with only one photoactive electrode (Table 3).

The behaviour of the photocurrent density is explained in terms of inter-electrodes separation in the DSCs with the different configurations here considered. In the adopted experimental conditions, the spacer interposed between the DSC electrodes as a frame has a fixed value of thickness (Figure 7). Given the variation of the total thickness of the electrodes in passing from *p*- and *n*-DSCs to *t*-DSC, the latter type of device, characterized by having the largest sum of electrodes thicknesses, will possess the thinnest electrolytic layer ( $l_{ele}$ ) with respect to *p*- and *n*-DSCs being  $l_{ele} (t\text{-type}) < l_{ele} (n\text{-type}) < l_{ele} (p\text{-type})$  (Figure 7). The electrical resistance of the electrolyte ( $R_{ele}$ ) will then diminish in the *t*-DSC with respect to the *p*- and *n*- devices being the nature (and the electrical resistivity  $\kappa_{ele}$ ) of the electrolyte the same in all the photoconversion devices here studied.<sup>72</sup> It is here recalled that  $R_{ele} = \kappa_{ele} \cdot l_{ele} / A_{ele}$  with  $A_{ele}$  representing the contact area at the interface electrode/electrolyte. By virtue of the

diminished resistance of the electrolyte in the *t*-DSC, it has to be expected an increase of the photocurrent density in going from the parent *n*- (or *p*)-type device to the tandem cell, as observed (Table 3).

Usually, EIS is the technique of election to analyse the ionic diffusion process taking place *in operando* condition. When *n*-type devices are measured, a separated semicircle due to the electrolyte diffusion could be evidenced at relatively low frequencies; yet, this is hardly distinguishable in *p*-type devices due to the fact that the charge transport/recombination phenomena have a longer characteristic time leading to superimposing of the two features, at least in the Nyquist's plot. The impedance spectra is even more puzzling when tandem devices are considered: indeed, when Pt is used as counter-electrode (CE) the characteristic time of the charge transfer at the CE/electrolyte interface is relatively low (ms scale) and a clearly separated features appears at higher frequencies; the replacement of the Pt film with a photoactive electrode (no matter in which geometry) leads to an increase of the characteristic time of the charge transfer process. EI spectra are reported in figure S6 in both Nyquist's and Bode's plot, but, unfortunately, definitive evidence could not be extracted from them (table S1).

The definitive recognition of the influence of spacer thickness on the current density of a DSC has been achieved when tandem cells were assembled with spacers having different thicknesses. In Table 3 for the *t*-DSCs there are two sets of data, each referring to a tandem device with a specific value of spacer thickness. The two different values of thickness were 15 and 25  $\mu\text{m}$  for the spacers here employed. As expected, it is observed a relatively poorer performance of photocurrent generation for the cell assembled with the thicker spacer due to the larger thickness of the electrolyte and the consequent higher resistance of the electrolytic layer. A further thinning of the thermoplastic polymer employed as spacer could improve the photoelectrochemical performance of the device but, unfortunately, such a thin film (< 15  $\mu\text{m}$ ) is not affordable, being not handy with our instrumentation.

The fill factor of the *t*-DSC is close to the one of the *n*-DSC (about 0.7) while the overall efficiency of the *t*-DSC ( $\eta = 1.88\%$ ) is higher than the corresponding *p*-DSC and *n*-DSC when the tandem device is illuminated from the photocathode side. This result is one of the highest ever reported for this type of device.<sup>26</sup> The illumination of the *t*-DSC from the side of the photoanode produced a weaker photoelectrochemical response being in this case  $J_{\text{sc}} = 3.2\text{ mA cm}^{-2}$  and  $\eta = 1.54\%$ . These results show that the photoelectrochemical response of the *t*-DSC is unsymmetrical with respect to the direction of irradiation (see Table 3).

**Table 3.** Photoelectrochemical parameters of *n*-, *p*- and *t*-DSC device from the profiles of Figure 6. Both sides of the *t*-DSC have been illuminated.

Device (photocathode material)	$V_{\text{oc}} /$ mV	$J_{\text{sc}} / \text{mA}$ $\text{cm}^{-2}$	FF / %	$\eta / \%$
<i>p</i> -DSC (NiO)	128	2.738	0.33	0.12
<i>p</i> -DSC (NZNC)	124	3.523	0.34	0.15
<i>n</i> -DSC	580	3.621	0.68	1.43
<i>t</i> -DSC (NZNC) # spacer thickness: 15 $\mu\text{m}$	678	4.198	0.66	1.88
<i>t</i> -DSC (NZNC) ## spacer thickness: 15 $\mu\text{m}$	682	2.800	0.66	1.26
<i>t</i> -DSC (NZNC) # spacer thickness: 25 $\mu\text{m}$	684	3.012	0.63	1.30
<i>t</i> -DSC (NZNC) ## spacer thickness: 25 $\mu\text{m}$	688	2.352	0.59	0.95

#Illuminated on cathode side

## Illuminated on anode side

In absence of electrolyte thickness effect, when the photoconversion performances of DSCs with one photoactive electrode (sensitized nanostructured NiO and TiO<sub>2</sub> for *p*- and *n*-DSCs, respectively) are compared, it is systematically found that *p*-DSCs produce smaller photocurrents than *n*-DSCs at analogous levels of light absorption<sup>17,90</sup> and, correspondingly, display lower overall efficiencies (see Table 3). A major cause of that is related to the occurrence of hole recombination at the NiO photoelectrode/electrolyte interface, a phenomenon that limits the effectiveness of hole photoinjection.<sup>16</sup> This is evidenced when the photoconversion performances of the *p*-DSC with NiO and NZNC as photocathodes are compared (Table 3). The presence of ZrO<sub>2</sub> in the nanocomposite, i.e. a non redox active component, affords the largest photocurrent in the corresponding *p*-DSC coherently with the intention of abating phenomena of hole recombination through the addition of ZrO<sub>2</sub> in the NiO matrix. Therefore, the general performance of a sensitized photocathode, either in a tandem device or in a *p*-type device, is limited by hole photoinjection in the cathode. In fact, the IPCE of the *t*-DSC is not the mere superposition of the corresponding *p*- and *n*-DSC external quantum efficiency spectra since the relative heights of the IPCE maxima of the *t*-DSC differ from the ones of the parent single photoelectrode cell. This is because *p*- and *n*-DSC have a common spectral region of photoelectrochemical activity due to the absorption of the redox couple I<sup>-</sup>/I<sub>3</sub><sup>-</sup> in the near UV ( $\lambda < 360$  nm).<sup>91–94</sup> At this regard the choice of a combination of dye-sensitizers with complementary absorption features in the *t*-DSC has not effect in the spectral region where redox shuttle is a strong light absorbing species.

## Conclusions

The NiO/ZrO<sub>2</sub> nanocomposites obtained via sintering of spray-deposited suspensions that contained preformed NiO and ZrO<sub>2</sub> nanoparticles resulted very attractive as photocathodic materials in *p*-DSCs. Spray-deposited NiO/ZrO<sub>2</sub> nanocomposites retained the crystalline structures of the parent nanoparticles of NiO and ZrO<sub>2</sub> and no formation of mixed oxides could be observed. In fact, the combined analysis of XRD patterns and SEM pictures demonstrated that spray-deposited NiO/ZrO<sub>2</sub> nanocomposites are solid solutions of ZrO<sub>2</sub> nanodomains embedded into a matrix of nanostructured NiO. The *p*-DSCs with nanocomposites photocathodes achieved regularly photoconversion efficiencies as high as 0.15% under irradiation with an AM 1.5G sun simulator when the cathodes were sensitized by P1 and I<sup>-</sup>/I<sub>3</sub><sup>-</sup> was redox shuttle. In particular, the largest photoconversion efficiency of 0.162 % for a *p*-DSC was measured when the nanocomposite photocathode had the the Zr/Ni molar ratio of 0.02. Such an optimal composition of the nanocomposite cathode was employed also for the production of photocathodes in *t*-DSCs with squaraine-sensitized TiO<sub>2</sub> as photoanodes. The resulting tandem device had a maximum conversion efficiency of 1.88 % and 4.2 mA cm<sup>-2</sup> as photocurrent density. To our knowledge these values are among the largest reported insofar for a *t*-DSC based on NiO and TiO<sub>2</sub> photoelectrodes when the sensitizers possess complementary absorption properties in the visible spectrum. Crucial was the choice of the thickness value for the TiO<sub>2</sub> anode since through the modulation of the anode thickness we could reach the exact matching between photoanodic and the (limiting) photocathodic current in the tandem device.



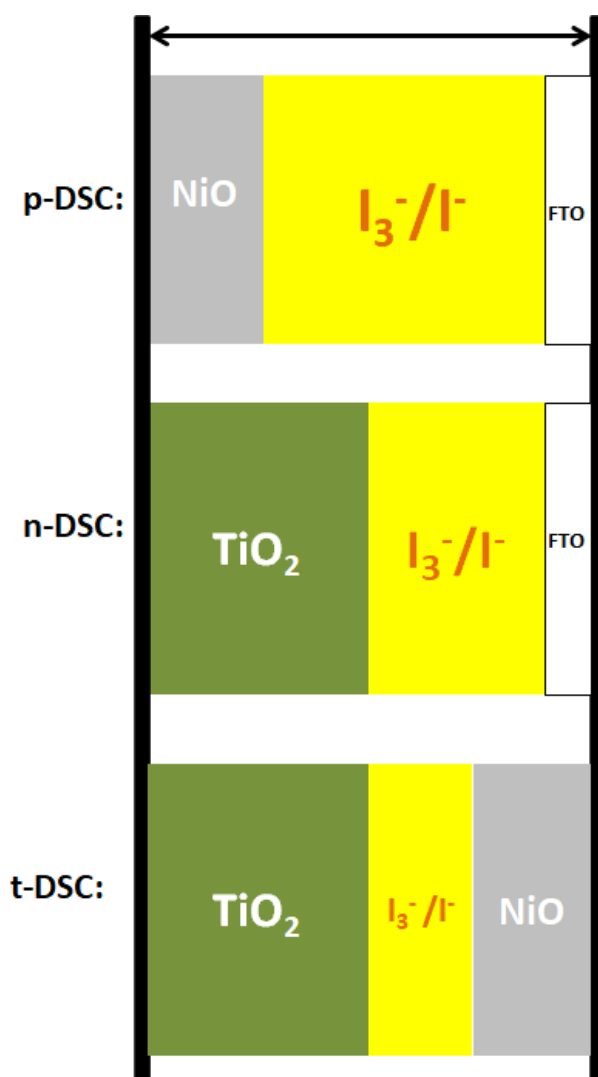


**Figure 7.** Schematic depiction of the DSC sections for the different configurations of cell. In passing from the DSC of (top) p- and (middle) n-type to the (bottom) DSC of t-type there is a progressive diminution of the electrolyte layer thickness given the fixed value of thickness (30  $\mu\text{m}$ ) for the spacer interposed between the electrodes substrates. In this representation at the back of all photoelectrodes the underlying layer of FTO is omitted for sake of simplicity.

#### Author Contributions

M. Bonomo, D. Dini and C. Barolo had the idea for this manuscript. C. Barolo provided the sensitizers. M. Bonomo, E.J. Ekoi and D.P. Dowling prepared and characterized the various nanocomposite electrodes. M. Bonomo and A.Y. Segura Zarate performed the photoelectrochemical characterization. A.G. Marrani performed XPS measurements. The manuscript was written with the contributions of all authors. All authors have given approval to the final version of the manuscript.

#### Conflicts of interest

There are no conflicts to declare.

#### Acknowledgements

D.D. acknowledges the financial supports from MIUR (Project PRIN 2017 with title “Novel Multilayered and Micro-Machined Electrode Nano-Architectures for Electrocatalytic Applications” - Prot. No. 2017YH9MRK) and from the University of Rome “La Sapienza” (Project ATENEO 2019, Prot. No. RM11916B756961CA). Moreover, authors thank the Center for Nanotechnology Applied to Engineering (CNIS) of the University of Rome “La Sapienza” for supporting the research and providing access to the DaVinci D8 diffractometer. Dr. Frederic Sauvage is kindly acknowledged for profitable discussion.

## Notes and references

- 1 B. O'Regan, M. Gratzel and M. Grätzel, *Nature*, 1991, **353**, 737–739.
- 2 A. Hagfeldt, G. Boschloo, L. Sun, L. Kloo and H. Pettersson, *Chem. Rev.*, 2010, **110**, 6595–6663.
- 3 R. Amadelli, R. Argazzi, C. A. Bignozzi and F. Scandola, *J. Am. Chem. Soc.*, 1990, **112**, 7099–7103.
- 4 J. Gong, K. Sumathy, Q. Qiao and Z. Zhou, *Review on dye-sensitized solar cells (DSSCs): Advanced techniques and research trends*, 2017, vol. 68.
- 5 M. Z. H. Khan, M. R. Al-Mamun, P. K. Halder and M. A. Aziz, *Renew. Sustain. Energy Rev.*, 2017, **71**, 602–617.
- 6 J. E. Moser, K. . Kalyanasundaram, S. . Ito, S. . Yanagida, S. Uchida and J. E. Moser, 2010, 403–456.
- 7 S. Wrede and H. Tian, *Phys. Chem. Chem. Phys.*, 2020, **22**, 13850–13861.
- 8 M. Hamadanian, J. Safaei-Ghomi, M. Hosseinpour, R. Masoomi and V. Jabbari, *Mater. Sci. Semicond. Process.*, , DOI:10.1016/j.mssp.2014.08.017.
- 9 N. T. R. N. Kumara, A. Lim, C. M. Lim, M. I. Petra and P. Ekanayake, *Renew. Sustain. Energy Rev.*, 2017, **78**, 301–317.
- 10 D. Dini, *Int. J. Mol. Sci.*, 2003, **4**, 291–300.
- 11 K. Kalyanasundaram, Ed., in *Dye-sensitized solar cells*, CRC Press, Lausanne, 2010, pp. 207–249.
- 12 S. Mozaffari, M. R. Nateghi and M. B. Zarandi, *Renew. Sustain. Energy Rev.*, 2017, **71**, 675–686.
- 13 S. Mathew, A. Yella, P. Gao, R. Humphry-Baker, B. F. E. Curchod, N. Ashari-Astani, I. Tavernelli, U. Rothlisberger, M. K. Nazeeruddin and M. Grätzel, *Nat. Chem.*, 2014, **6**, 242–247.
- 14 U. Bach, D. Lupo, P. Comte, J. E. Moser, F. Weissörtel, J. Salbeck, H. Spreitzer and M. Grätzel, *Nature*, 1998, **395**, 583–585.
- 15 M. Bonomo, D. Dini and F. Decker, *Front. Chem.*, 2018, **6**, 601.
- 16 A. Nattestad, I. Perera and L. Spiccia, *J. Photochem. Photobiol. C Photochem. Rev.*, 2016, **28**, 44–71.
- 17 J. He, H. Lindström, A. Hagfeldt and S.-E. Lindquist, *Sol. Energy Mater. Sol. Cells*, 2000, **62**, 265–273.
- 18 H. Choi, T. Hwang, S. Lee, S. Nam, J. Kang, B. Lee and B. Park, *J. Power Sources*, 2015, **274**, 937.
- 19 A. De Vos, *J. Phys. D. Appl. Phys.*, 1980, **13**, 839–846.
- 20 S. Sumikura, S. Mori, S. Shimizu, H. Usami and E. Suzuki, *J. Photochem. Photobiol. A Chem.*, 2008, **199**, 1.
- 21 Y. Xu, T. Gong and J. N. Munday, *Sci. Rep.*, 2015, **5**, 13536.
- 22 W. Shockley and H. J. Queisser, *J. Appl. Phys.*, 1961, **32**, 510–519.
- 23 A. G. Marrani, V. Novelli, S. Sheehan, D. P. Dowling and D. Dini, *ACS Appl. Mater. Interfaces*, 2014, **6**, 143–152.
- 24 C. J. Wood, M. Cheng, C. A. Clark, R. Horvath, I. P. Clark, M. L. Hamilton, M. Towrie, M. W. George, L. Sun, X. Yang and E. A. Gibson, *J. Phys. Chem. C*, 2014, **118**, 16536–16546.
- 25 C. J. Wood, G. H. Summers and E. A. Gibson, *Chem. Commun.*, 2015, **51**, 3915.
- 26 A. Nattestad, A. J. Mozer, M. K. R. Fischer, Y.-B. Cheng, A. Mishra, P. Bauerle, U. Bach, P. Bäuerle and U. Bach, *Nat. Mater.*, 2010, **9**, 31–35.
- 27 G. Y. Yang, M. Hanack, Y. W. Lee, D. Dini and J. F. Pan, *Adv. Mater.*, 2005, **17**, 875–879.
- 28 K. Kakiage, Y. Aoyama, T. Yano, K. Oya, J. I. Fujisawa and M. Hanaya, 2015, **51**, 15894–15897.
- 29 A. Yella, H.-W. Lee, H. N. Tsao, C. Yi, A. K. Chandiran, M. K. Nazeeruddin, E. W.-G. Diau, C.-Y. Yeh, S. M. Zakeeruddin and M. Gratzel, *Science (80-. )*, 2011, **334**, 629-.
- 30 I. R. Perera, T. Daeneke, S. Makuta, Z. Yu, Y. Tachibana, A. Mishra, P. Bäuerle, C. A. Ohlin, U. Bach and L. Spiccia, *Angew. Chemie - Int. Ed.*, 2015, **54**, 3758–3762.
- 31 M. Borgström, E. Blart, G. Boschloo, E. Mukhtar, A. Hagfeldt, L. Hammarström and F. Odobel, *J. Phys. Chem. B*, 2005, **109**, 22928–22934.
- 32 F. Le Pleux, L.; Smeigh, A.L.; Gibson, E.; Pellegrin, Y.; Blart, E.; Boschloo, G.; Hagfeldt, A.; Hammarström, L.; Odobel, *Energy Environ. Sci.*, 2011, **4**, 2075–2084.
- 33 M. Bonomo, C. Magistris, R. Buscaino, A. Fin, C. Barolo and D. Dini, *ChemistrySelect*, 2018, **3**, 1066–1075.
- 34 Y. Farré, M. Raissi, A. Fihey, Y. Pellegrin, E. Blart, D. Jacquemin and F. Odobel, *ChemSusChem*, 2017, **10**, 2618–2625.
- 35 Y. Farré, M. Raissi, A. Fihey, Y. Pellegrin, E. Blart, D. Jacquemin and F. Odobel, *Dye. Pigment.*, 2017, **148**, 154–166.
- 36 H. Ye, L. Shen, S. Zhang, X. Li, F. Yu, R. Diau and J. Hua, *ACS Omega*, 2018, **3**, 14448–14456.
- 37 T. Daeneke, Z. Yu, G. P. Lee, D. Fu, N. W. Duffy, S. Makuta, Y. Tachibana, L. Spiccia, A. Mishra, P. Bäuerle and U. Bach, *Adv. Energy Mater.*, 2015, **5**, 1401387.
- 38 Z. Huang, G. Natu, Z. Ji, M. He, M. Yu and Y. Wu, *J. Phys. Chem. C*, 2012, **116**, 26239–26246.

- 39 E. Benazzi, J. Mallows, G. H. Summers, F. A. Black and E. A. Gibson, *J. Mater. Chem. C*, 2019, **7**, 10409–10445.
- 40 D. Pumiglia, M. Giustini, D. Dini, F. Decker, A. Lanuti, S. Mastroianni, S. Veyres and F. Caprioli, *ChemElectroChem*, 2014, **1**, 1388–1394.
- 41 M. Bonomo, A. Carella, F. Borbone, L. Rosato, D. Dini and L. Gontrani, *Dye. Pigment.*, 2020, **175**, 108140.
- 42 P. Goel, S. Sundriyal, V. Shrivastav, S. Mishra, D. P. Dubal, K. H. Kim and A. Deep, *Nano Energy*, 2021, **80**, 105552.
- 43 P. Mahajan, R. Datt, W. Chung Tsoi, V. Gupta, A. Tomar and S. Arya, *Coord. Chem. Rev.*, 2021, **429**, 213633.
- 44 D. Di Girolamo, F. Matteocci, M. Piccinni, A. Di Carlo and D. Dini, *Sol. Energy Mater. Sol. Cells*, 2019, 110288.
- 45 D. Di Girolamo, F. Di Giacomo, F. Matteocci, A. G. Marrani, D. Dini, A. Abate and D. Di Girolamo, *Chem. Sci.*, 2020, **11**, 7746–7759.
- 46 J. Föhlinger, S. Maji, A. Brown, E. Mijangos, S. Ott and L. Hammarström, *J. Phys. Chem. C*, 2018, **122**, 13902–13910.
- 47 S. Biswas, J. Husek, S. Londo and L. R. Baker, *J. Phys. Chem. Lett.*, 2018, **9**, 5047–5054.
- 48 C. J. Flynn, S. M. McCullough, L. Li, C. L. Donley, Y. Kanai and J. F. Cahoon, *J. Phys. Chem. C*, 2016, **120**, 16568–16576.
- 49 G. Boschloo and A. Hagfeldt, *J. Phys. Chem. B*, 2001, **105**, 3039–3044.
- 50 C. J. Wood, G. H. Summers, C. A. Clark, N. Kaeffer, M. Braeutigam, L. R. Carbone, L. D’Amario, K. Fan, Y. Farré, S. Narbey, F. Oswald, L. A. Stevens, C. D. J. Parmenter, M. W. Fay, A. La Torre, C. E. Snape, B. Dietzek, D. Dini, L. Hammarström, Y. Pellegrin, F. Odobel, L. Sun, V. Artero and E. A. Gibson, *Phys. Chem. Chem. Phys.*, 2016, **18**, 10727–10738.
- 51 L. D’Amario, R. Jiang, U. B. Cappel, E. A. Gibson, G. Boschloo, H. Rensmo, L. Sun, L. Hammarström and H. Tian, *ACS Appl. Mater. Interfaces*, 2017, **9**, 33470–33477.
- 52 S. Uehara, S. Sumikura, E. Suzuki and S. Mori, *Energy Environ. Sci.*, 2010, **3**, 641.
- 53 G. Natu, Z. Huang, Z. Ji and Y. Wu, *Langmuir*, 2012, **28**, 950–956.
- 54 C. J. Flynn, S. M. McCullough, E. Oh, L. Li, C. C. Mercado, B. H. Farnum, W. Li, C. L. Donley, W. You, A. J. Nozik, J. R. McBride, T. J. Meyer, Y. Kanai and J. F. Cahoon, *ACS Appl. Mater. Interfaces*, 2016, **8**, 4754–4761.
- 55 N. T. Z. Potts, T. Sloboda, M. Wächter, R. A. Wahyuno, V. D’Annibale, B. Dietzek, U. B. Cappel and E. A. Gibson, *J. Chem. Phys.*, 2020, **153**, 184704.
- 56 M. Bonomo, D. Saccone, C. Magistris, C. Barolo, L. Ciná, A. Di Carlo and D. Dini, *J. Electrochem. Soc.*, 2017, **164**, H1099–H1111.
- 57 L. Favereau, Y. Pellegrin, L. Hirsch, A. Renaud, A. Planchat, E. Blart, G. Louarn, L. Cario, S. Jovic, M. Boujtita and F. Odobel, *Adv. Energy Mater.*, 2017, **7**, 1601776.
- 58 M. Bonomo, D. Dini, A. G. Marrani and R. Zononi, *Colloids Surfaces A Physicochem. Eng. Asp.*, 2017, **532**, 464–471.
- 59 X. L. X. L. Zhang, F. Huang, A. Nattestad, K. Wang, D. Fu, A. Mishra, P. Bäuerle, U. Bach and Y.-B. Cheng, *Chem. Commun.*, 2011, **47**, 4808–4810.
- 60 M. Bonomo, D. Di Girolamo, M. Piccinni, D. P. Dowling and D. Dini, *Nanomaterials*, , DOI:10.3390/nano10010167.
- 61 M. Bonomo, P. Mariani, F. Mura, A. Di Carlo and D. Dini, *J. Electrochem. Soc.*, 2019, **166**, D290–D300.
- 62 P. Qin, H. Zhu, T. Edvinsson, G. Boschloo, A. Hagfeldt and L. Sun, *J. Am. Chem. Soc.*, 2008, **130**, 8570–8571.
- 63 N. Li, E. A. Gibson, P. Qin, G. Boschloo, M. Gorlov, A. Hagfeldt and L. Sun, *Adv. Mater.*, 2010, **22**, 1759–1762.
- 64 E. A. Gibson, M. Awais, D. Dini, D. P. Dowling, M. T. Pryce, J. G. Vos, G. Boschloo and A. Hagfeldt, *Pccp*, 2013, **15**, 2411–2420.
- 65 P. Qin, M. Linder, T. Brinck, G. Boschloo, A. Hagfeldt and L. Sun, *Adv. Mater.*, 2009, **21**, 2993–2996.
- 66 O. A. Graeve, in *Ceramic and Glass Materials: Structure, Properties and Processing*, 2008, pp. 169–197.
- 67 Y. Liu, J. Goebel and Y. Yin, *Chem. Soc. Rev.*, 2013, **42**, 2610.
- 68 T. P. Otroshchenko, A. O. Turakulova, V. A. Voblikova, L. V. Sabitova, S. V. Kutsev and V. V. Lunin, *Russ. J. Phys. Chem. A*, 2013, **87**, 1804–1808.
- 69 M. Bonomo, N. Barbero, F. Matteocci, A. Di Carlo, C. Barolo and D. Dini, *J. Phys. Chem. C*, 2016, **120**, 16340–16353.
- 70 J. Park, N. Barbero, J. Yoon, E. Dell’Orto, S. Galliano, R. Borrelli, J.-H. Yum, D. Di Censo, M. Grätzel, M. K. Nazeeruddin, C. Barolo and G. Viscardi, *Phys. Chem. Chem. Phys.*, 2014, **16**, 24173–24177.
- 71 S. Sheehan, G. Naponiello, F. Odobel, D. P. Dowling, A. Di Carlo and D. Dini, *J. Solid State Electrochem.*, 2015, **19**, 975–986.
- 72 M. Bonomo, G. Naponiello, I. Venditti, V. Zardetto, A. Di Carlo and D. Dini, *J. Electrochem. Soc.*, 2017, **164**, H137–H147.
- 73 J. H. Scofield, *J. Electron Spectros. Relat. Phenomena*, 1976, **8**, 129–137.
- 74 P. Qin, J. Wiberg, E. A. Gibson, M. Linder, L. Li, T. Brinck, A. Hagfeldt, B. Albinsson and L. Sun, *J. Phys. Chem. C*, 2010, **114**, 4738–4748.
- 75 P. Mariani, L. Vesce and A. Di Carlo, *Semicond. Sci. Technol.*, 2015, **30**, 104003.
- 76 R. Cisneros, M. Beley and F. Lapique, *Phys. Chem. Chem. Phys.*, 2016, **18**, 9645–9651.
- 77 L. Tian, R. Tyburski, C. Wen, R. Sun, M. Abdallah, J. Huang, L. D’Amario, G. Boschloo, L. Hammarström and H. Tian, *J. Am. Chem. Soc.*, 2020, **142**, 18668–18678.
- 78 A. P. Grosvenor, M. C. Biesinger, R. S. C. Smart and N. S. McIntyre, *Surf. Sci.*, 2006, **600**, 1771–1779.
- 79 I. Preda, R. J. O. Mossaneck, M. Abbate, L. Alvarez, J. Méndez, A. Gutiérrez and L. Soriano, *Surf. Sci.*, 2012, **606**, 1426–1430.
- 80 M. A. Van Veenendaal and G. A. Sawatzky, *Phys. Rev. Lett.*, 1993, **70**, 2459–2462.
- 81 R. J. O. Mossaneck, I. Preda, M. Abbate, J. Rubio-Zuazo, G. R. Castro, A. Vollmer, A. Gutiérrez and L. Soriano, *Chem. Phys. Lett.*, 2011, **501**, 437–441.
- 82 L. Soriano, I. Preda, A. Gutiérrez, S. Palacín, M. Abbate and A. Vollmer, *Phys. Rev. B - Condens. Matter Mater. Phys.*, 2007, **75**, 1–4.
- 83 J. Van Elp, H. Eskes, P. Kuiper and G. A. Sawatzky, *Phys. Rev. B*, 1992, **45**, 1612–1622.
- 84 P. Kuiper, G. Kruizinga, J. Ghijsen, G. A. Sawatzky and H. Verweij, *Phys. Rev. Lett.*, 1989, **62**, 221–224.
- 85 A. Thissen, D. Ensling, F. J. F. Madrigal, W. Jaegermann, R. Alcántara, P. Lavela and J. L. Tirado, *Chem. Mater.*, 2005, **17**, 5202–5208.
- 86 M. Bonomo, A. G. A. G. Marrani, V. Novelli, M. Awais, D. P. D. P. Dowling, J. G. J. G. Vos and D. Dini, *Appl. Surf. Sci.*, 2017, **403**, 441–447.

- 87 H. Li, J. I. J. Choi, W. Mayr-Schmölzer, C. Weilach, C. Rameshan, F. Mittendorfer, J. Redinger, M. Schmid and G. Rupprechter, *J. Phys. Chem. C*, 2015, **119**, 2462–2470.
- 88 P. Mani, S. V. Nair and M. Shanmugam, *Emergent Mater.*, 2020, **3**, 117–124.
- 89 G. H. Summers and E. A. Gibson, *ChemPhotoChem*, 2018, **2**, 498–506.
- 90 A. Nattestad, M. Ferguson, R. Kerr, Y.-B. Cheng and U. Bach, *Nanotechnology*, 2008, **19**, 295304.
- 91 E. A. Gibson, L. Le Pleux, J. Fortage, Y. Pellegrin, E. Blart, F. Odobel, A. Hagfeldt and G. Boschloo, *Langmuir*, 2012, **28**, 6485–6493.
- 92 Z. Hongjun, A. Hagfeldt and G. Boschloo, *J. Phys. Chem. C*, 2007, **111**, 17455–17458.
- 93 G. Boschloo and A. Hagfeldt, *Acc. Chem. Res.*, 2009, **42**, 1819–1826.
- 94 M. Bonomo, A. Di Carlo and D. Dini, *J. Electrochem. Soc.*, 2018, **165**, H889–H896.